



# Photocatalytic H<sub>2</sub>O<sub>2</sub> production driven by cyclodextrin-pyrimidine polymer in a wide pH range without electron donor or oxygen aeration

Chengcheng Chu<sup>a,b</sup>, Qiuju Li<sup>a,b</sup>, Wei Miao<sup>a,b</sup>, Hehe Qin<sup>a,b</sup>, Xinru Liu<sup>a,b</sup>, Ducheng Yao<sup>a,b</sup>, Shun Mao<sup>a,b,\*</sup>

<sup>a</sup> College of Environmental Science and Engineering, Biomedical Multidisciplinary Innovation Research Institute, Shanghai East Hospital, State Key Laboratory of Pollution Control and Resource Reuse, Tongji University, 1239 Siping Road, Shanghai 200092, China

<sup>b</sup> Shanghai Institute of Pollution Control and Ecological Security, Shanghai 200092, China

## ARTICLE INFO

### Keywords:

Polymer catalyst  
Photocatalytic H<sub>2</sub>O<sub>2</sub> production  
PH adaptability, water oxidation reaction  
Oxygen reduction reaction

## ABSTRACT

Photocatalytic H<sub>2</sub>O<sub>2</sub> generation has drawn growing attention for on-site H<sub>2</sub>O<sub>2</sub> production. However, current photocatalytic systems still need organic electron donor, oxygen aeration, and acidic pH to elevate the production efficiency. We report a crosslinking polymer catalyst constructed by β-cyclodextrin aldehyde and 4-amino-6-hydroxy-2-mercaptopyrimidine to address the above challenges. This novel catalyst achieves an outstanding yield rate of 557.2 μM g<sup>-1</sup> h<sup>-1</sup> for photocatalytic H<sub>2</sub>O<sub>2</sub> production in pure water and can maintain its performance over a wide pH range (1–11) without electron donor or oxygen aeration. The mechanism investigation shows that the high generation performance is attributed to the mutual promotion of water photooxidation and oxygen photoreduction. Moreover, this catalyst is demonstrated for in situ sterilization in various water bodies under visible light irradiation. The reported polymer photocatalyst addresses some of the obstacles in photocatalytic H<sub>2</sub>O<sub>2</sub> generation, and will promote practical applications of H<sub>2</sub>O<sub>2</sub> generation from solar energy.

## 1. Introduction

As a valuable green reagent, hydrogen peroxide (H<sub>2</sub>O<sub>2</sub>) is widely used in bleaching, chemical industry, liquid fuel, sewage treatment, and others [1–3]. At present, anthraquinone (AQ) method is still the mainstream process for mass production of H<sub>2</sub>O<sub>2</sub> [4,5]. However, many new processes, especially on-site production of H<sub>2</sub>O<sub>2</sub>, are being developed to solve the high cost and environmental safety problems from the production and transportation of H<sub>2</sub>O<sub>2</sub> [6–8]. Using sustainable sunlight as energy input, photocatalysis process can directly convert H<sub>2</sub>O and O<sub>2</sub> into H<sub>2</sub>O<sub>2</sub>, showing promises for continuous on-site production of H<sub>2</sub>O<sub>2</sub> [9,10].

Inorganic semiconductors have been reported for photocatalytic H<sub>2</sub>O<sub>2</sub> production, however, the generated H<sub>2</sub>O<sub>2</sub> is usually adsorbed on the surface of the catalyst, which leads to further reaction of photo-generated electrons and adsorbed H<sub>2</sub>O<sub>2</sub>, resulting in high H<sub>2</sub>O<sub>2</sub> decomposition rate and low overall H<sub>2</sub>O<sub>2</sub> production efficiency [11–13]. Organic polymer catalysts represented by graphitic carbon nitride (g-C<sub>3</sub>N<sub>4</sub>) recently become a hot research topic for photocatalytic H<sub>2</sub>O<sub>2</sub>

production [5,14,15]. With suitable band structure, H<sub>2</sub>O<sub>2</sub> can be generated over g-C<sub>3</sub>N<sub>4</sub> through selective two-electron oxygen reduction and the generated H<sub>2</sub>O<sub>2</sub> is easily desorbed from the surface [16]. Although g-C<sub>3</sub>N<sub>4</sub> shows high potentials for photocatalytic H<sub>2</sub>O<sub>2</sub> generation [17–25]; current catalyst systems still face the following challenges: (i) the need of organic electron donor to alleviate fast charge recombination; (ii) the need of acidic pH condition to stabilize H<sub>2</sub>O<sub>2</sub>; and (iii) the need of oxygen atmosphere for high oxygen reduction reaction (ORR) rate. Therefore, novel catalyst system that can address the above obstacles is highly needed to realize the efficient photocatalytic H<sub>2</sub>O<sub>2</sub> production under practical conditions.

Recently, new organic polymer semiconductors including covalent triazine frameworks (CTFs), covalent organic framework (COF), and donor-acceptor (D-A) conjugated polymers have been reported for photocatalytic H<sub>2</sub>O<sub>2</sub> production [26–30]. The surface chemistry and band structure of metal-free polymer photocatalysts can be designed and modulated, which benefits the selective production H<sub>2</sub>O<sub>2</sub> with low H<sub>2</sub>O<sub>2</sub> decomposition rate. For instance, D-A type resorcinol-formaldehyde (RF) crosslinked resin shows low band gap (~2.0 eV) and light

\* Corresponding author at: College of Environmental Science and Engineering, Biomedical Multidisciplinary Innovation Research Institute, Shanghai East Hospital, State Key Laboratory of Pollution Control and Resource Reuse, Tongji University, 1239 Siping Road, Shanghai 200092, China.

E-mail address: [shunmao@tongji.edu.cn](mailto:shunmao@tongji.edu.cn) (S. Mao).

<https://doi.org/10.1016/j.apcatb.2022.121485>

Received 7 March 2022; Received in revised form 2 May 2022; Accepted 5 May 2022

Available online 10 May 2022

0926-3373/© 2022 Elsevier B.V. All rights reserved.

absorption up to 700 nm wavelength, which can generate  $\text{H}_2\text{O}_2$  through ORR process from pure water [31]. The C-N-based organic polymer containing P and O shows a two-channel reaction process of both water oxidation reaction (WOR) and ORR for  $\text{H}_2\text{O}_2$  evolution, in which the P and O sites capture the charges and inhibit the recombination of carriers [32]. In another study, the hydrophobic cavities of per-6-thio- $\beta$ -cyclodextrin (SH- $\beta$ -CD) have been demonstrated to serve as "transfer channel", which promote the diffusion of  $\text{O}_2$  to the active site for enhanced ORR process in  $\text{H}_2\text{O}_2$  production [33]. However, most of these organic catalysts require expensive precursors or complex synthetic routes. Moreover, the reported photocatalytic systems cannot sufficiently produce  $\text{H}_2\text{O}_2$  under neutral/alkaline pH condition and have low  $\text{H}_2\text{O}_2$  production efficiency in complex real water environment, which limit the practical applications of photocatalytic  $\text{H}_2\text{O}_2$  production.

Inspired by the above studies, we report a new cyclodextrin-pyrimidine (CDA) polymer catalyst through calcination of  $\beta$ -cyclodextrin aldehyde (ACD) and 4-amino-6-hydroxy-2-mercaptopyrimidine (AHMP) at low temperature to simultaneously promote the ORR and WOR process for highly efficient  $\text{H}_2\text{O}_2$  production. This polymer exhibits

excellent light absorption capacity with absorption range at the visible and near-infrared region (420–800 nm). Previous studies show that pyrimidines can retain the original structure and form oligomers with periodic structure by thermal condensation at low temperature [34,35]. As shown in Fig. 1, the introduced ACD will crosslink with AHMP and disrupts the periodic structure of AHMP-based oligomer to enhance its photocatalytic activity. At the same time, it can also serve as the oxygen delivery channel for  $\text{H}_2\text{O}_2$  generation at adjacent active sites. The optimal band structure of CDA leads to high WOR activity, which addresses the issues of organic electron donor and pH adjustment in most photocatalytic  $\text{H}_2\text{O}_2$  production systems. Without electron donor and pH adjustment, the CDA polymer exhibits outstanding  $\text{H}_2\text{O}_2$  yield rate of  $557.2 \mu\text{mol g}^{-1} \text{L}^{-1}$  under air atmosphere, superior to some of the best reported  $\text{H}_2\text{O}_2$  evolution catalysts (Fig. 1). The mechanism study indicates that the  $\text{H}_2\text{O}_2$  generation proceeds through a two-channel reaction pathway containing 2-electron ORR and 2-electron WOR. To demonstrate the applicability of CDA for in-situ generation of  $\text{H}_2\text{O}_2$ , the sterilization application of in-situ produced  $\text{H}_2\text{O}_2$  with CDA was demonstrated in natural water (tap water, lake water, river water) and secondary effluent from waste water treatment plant. This

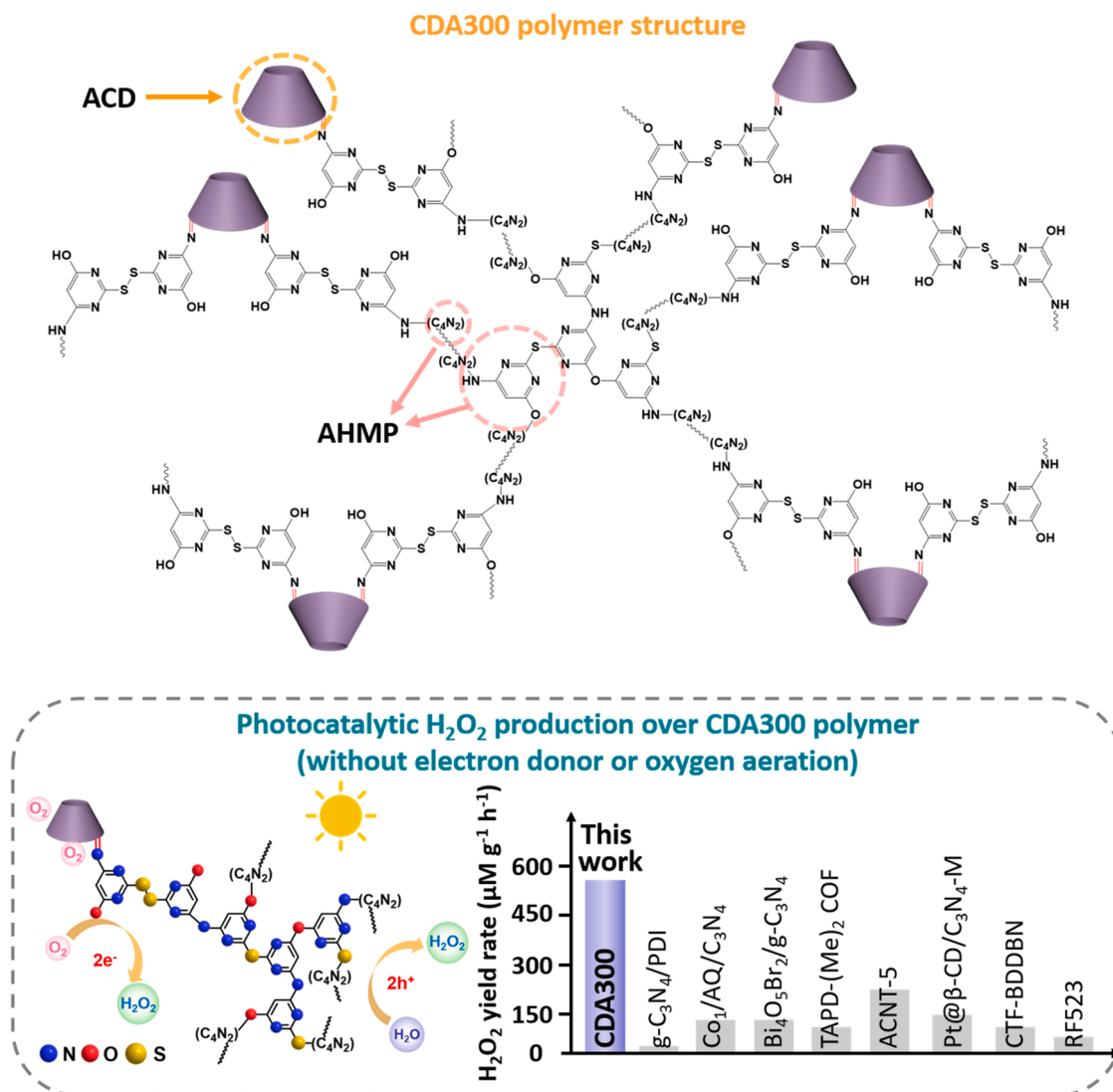


**Fig. 1.** Polymeric structure and photocatalytic  $\text{H}_2\text{O}_2$  production performance of CDA300. Schematic diagram of the proposed structure of CDA300. The two-channel reaction pathway contains two-electron ORR and two-electron WOR. The performance comparison between CDA300 and other representative catalysts for photocatalytic  $\text{H}_2\text{O}_2$  production under visible light irradiation (without electron donor). PDI stands for pyromellitic diimide, AQ stands for anthraquinone, TAPD stands for  $\text{N,N,N',N'}$ -tetrakis(4-aminophenyl)-1,4-phenylenediamine, ACNT stands for alkalized carbon nitride nanotubes, BDDBN stands for 4,4'-(buta-1,3-diene-1,4-diyl) dibenzonitrile, and RF stands for resorcinol-formaldehyde.

photocatalytic system maintains excellent  $\text{H}_2\text{O}_2$  evolution performance in these water bodies and displays remarkable sterilization capacity. It is believed that this new polymer catalyst will promote the development of highly efficient and applicable photocatalytic system for  $\text{H}_2\text{O}_2$  production.

## 2. Experimental section

### 2.1. Synthesis of CDA

The cross-linked polymer composed of ACD and AHMP was synthesized by the similar method reported in our previous study [36]. In the synthesis process, 0.3 g ACD was dissolved in water (20 mL), followed by addition of 0.3 g AHMP. The mixture was stirred for 10 min at 60 °C and the resultant suspension was collected and washed with DI water and ethanol for three times and dried in vacuum at 60 °C, which was denoted as CDA. Then, the dried CDA was calcined in a muffle furnace at different temperature (250, 300, or 350 °C) for 2 h with a heating rate of 5 °C min<sup>-1</sup>. The final products were washed and dried, and labeled as CDAX (where x represents the annealing temperature). For comparison, AHMP300 catalyst was prepared by the polymerization of pure AHMP at 300 °C. The details of catalyst characterizations, electrochemical tests,

and simulations are shown in the [Supplementary Information](#).

### 2.2. Photocatalytic production of $\text{H}_2\text{O}_2$

In a typical experiment, 10 mg catalyst was dispersed in 40 mL ultrapure water. Before each test, the mixture was ultrasonicated for 5 min and stirred vigorously at 900 rpm under dark condition for 15 min. The visible light source was supplied by a 300 W Xe lamp (Perfectlight, PLS-SXE300) with a 420 nm cutoff filter. In the photoirradiation process, 2 mL solution was collected and filtered at every 10 min. The amount of generated  $\text{H}_2\text{O}_2$  was measured by the standard iodimetry method. All photocatalysis tests were performed in air and at natural pH unless otherwise specified. In the disinfection experiment, natural water was used as the solvent. The basic water parameters of lake water and secondary effluent were listed in [Table S3](#). The reaction condition of disinfection experiment was the same as photocatalytic  $\text{H}_2\text{O}_2$  production experiment. After 60 min of photoirradiation, 3 mL water sample was collected for cultivation, and the number of bacteria was recorded to test the bactericidal effect.

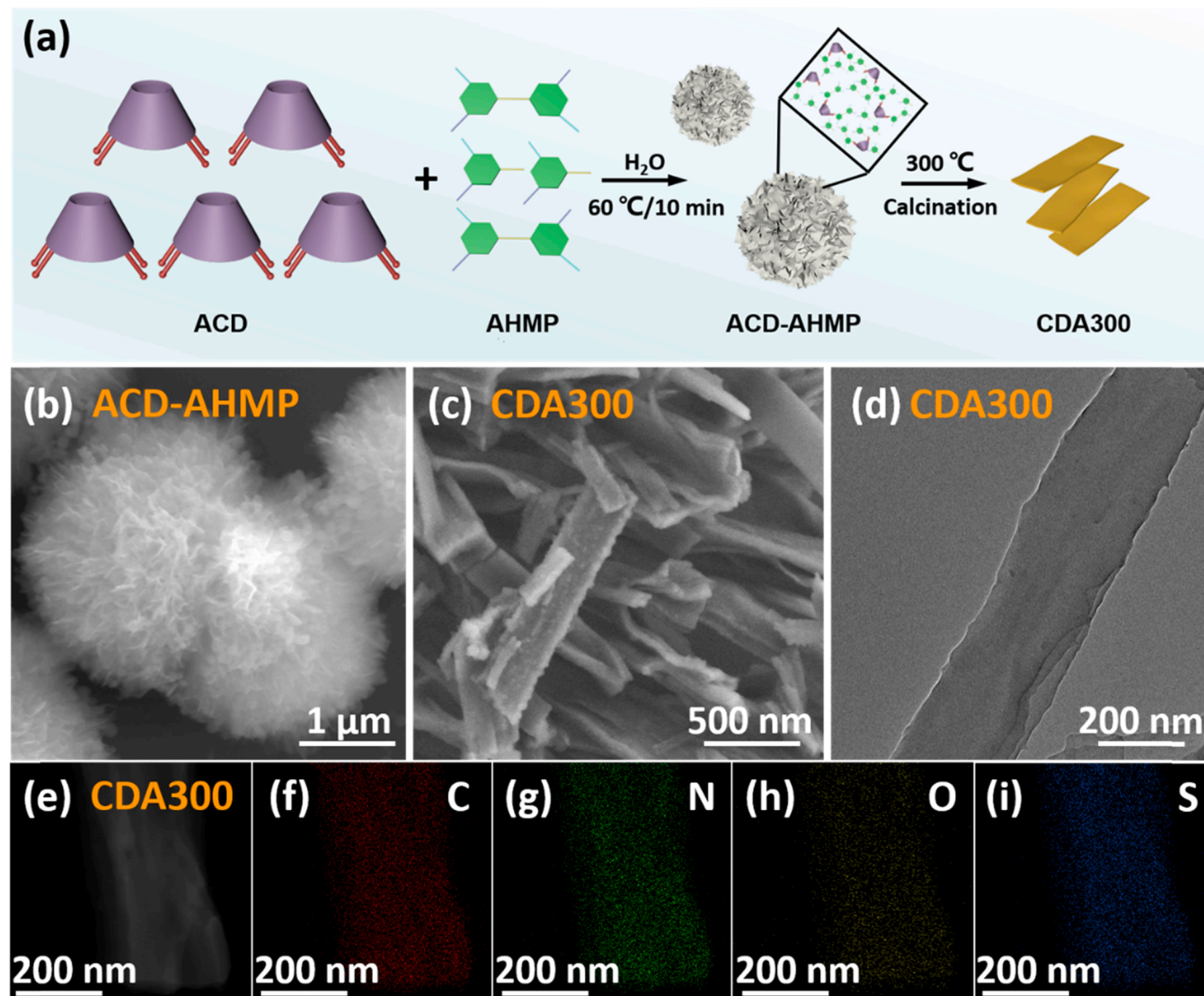


**Fig. 2.** Synthesis process and structure characterizations of CDA300. (a) Two-step synthetic process of CDA300. (b, c) SEM images of ACD-AHMP and CDA300. (d) TEM image and (e-i) EDS element mapping results of CDA300.



### 3. Results and discussion

#### 3.1. Structure of CDA

As displayed in Fig. 2a, CDA polymer was synthesized through two-step reactions. In the first step, well-formed cyclodextrin-pyrimidine (ACD-AHMP) nanoflower was obtained [36]. In this process, part of AHMP molecules formed dimers due to the disulfide bonds formed by sulfhydryl oxidation, and then underwent Schiff-base reaction with ACD to produce ACD-AHMP cross-linked product. The synthesis process of this cross-linked product is shown in Fig. S1. In the second step, through low temperature polycondensation at 300 °C, the cross-linked products and uncross-linked AHMP were further condensed to form polymer network CDA, which showed a nanobelt morphology.

The morphology evolution from ACD-AHMP to CDA during low-temperature calcination and the elemental distributions of produced CDA were studied by scanning electron microscope (SEM) and transmission electron microscope (TEM) imaging. As shown in Fig. 2b, the ACD-AHMP exhibits nanoflower morphology. Interestingly, upon thermal polymerization, this nanoflower structure collapses and transforms to a nanobelt structure (Fig. 2c-d). Fig. S2 shows the SEM images of CDA250 and CDA300, which both exhibit nanobelt structure, while CDA350 shows some irregular nanobelt structures due to deep polymerization between the precursors. The above results reveal that the crosslinking structure formed between ACD and AHMP guides the formation of nanobelt structure of CDA during pyrolysis process. The energy dispersive X-ray spectroscopy (EDS) mapping (Fig. 2e-i) indicates that C, N, O, and S elements are uniformly distributed over the whole nanobelt, which further confirms the successful construction of polymer network comprised by ACD and AHMP. Fig. S3 reveals that CDA300 with uniform nanobelt structure shows higher Brunauer-Emmett-Teller (BET) surface area ( $17.4 \text{ m}^2/\text{g}$ ) than that of bulk AHMP300 ( $9.2 \text{ m}^2/\text{g}$ ).

X-ray diffraction (XRD) patterns of the synthesized catalysts are shown in Fig. S4a. The characteristic peaks of AHMP are found in the XRD patterns of ACD-AHMP, indicating that the excess uncrosslinked AHMP is adsorbed in the crosslinked network. After low-temperature calcination, the CDA samples show two broad peaks at  $14.5^\circ$  and  $26.5^\circ$ , which are related to the layer stacking structure of CDA [32,37,38]. The disappearance of AHMP characteristic peaks reveals that the crystalline AHMP is condensed during thermal polymerization and eventually forms amorphous organic polymer. The Raman spectra also confirm the carbonized polymer structure of CDA300. As shown in Fig. S4b, the Raman spectrum of ACD-AHMP show characteristic bands of the stretching mode of AHMP. After calcination, D band (at  $1340 \text{ cm}^{-1}$ ) and G band (at  $1556 \text{ cm}^{-1}$ ) are found the spectrum of CDA300. The G band represents the in-plane stretching vibration of  $\text{sp}^2$  C atoms; while the D band is associated with disordered and defect-induced carbon structures [39,40].

The attenuated total reflectance Fourier transform infrared spectroscopy (ATR-FTIR) was used to further study the structural change of the catalyst during polymerization process (Fig. S4c). The CDA250 and CDA300 retain the characteristic peaks from ACD and AHMP, in which the  $1200\text{--}1700 \text{ cm}^{-1}$  band is the breathing mode of heterocyclic CN in AHMP,  $3435 \text{ cm}^{-1}$  band is the -OH group, and  $1043 \text{ cm}^{-1}$  band is the C-O-C bond in ACD, respectively [36,41,42]. After thermal calcination, a new band located at  $1371 \text{ cm}^{-1}$  is found in CDA300 and CDA350, which can be attributed to the C-N bond formed by the polymerization process [32]. The presence of C=S bond ( $1180 \text{ cm}^{-1}$ ) in CDA250 suggests that some AHMP exists in the thione form [43]. In contrast, in CDA300 and CDA350 samples, the C=S bond almost disappears, which further confirms the condensation process.

From the solid-state  $^{13}\text{C}$  NMR spectrum (Fig. S4d), the characteristic signals of both ACD and AHMP are found in CDA300 [32,44,45]. After polymerization, a new peak located at 151.3 ppm (corresponding to C=C) appears, and the peak at 82.9 ppm from ACD becomes broader and slightly shifts, which indicates that ACD in CDA300 is slightly

carbonized [39]. Thermo-gravimetric (TG) analysis was executed to study the thermal stability and calcination process of ACD-AHMP. As shown in Fig. S5, the ACD-AHMP losses  $\sim 8\%$  weight below  $100^\circ\text{C}$  due to the loss of adsorbed water; then, it begins to decompose at  $200^\circ\text{C}$  and shows  $\sim 11\%$  weight loss at  $300^\circ\text{C}$ , corresponding to the carbonization of ACD and oligomerization between AHMP. The element analysis (EA) was conducted to investigate the elemental composition change from ACD-AHMP to CDA300. As shown in Table S1, compared with ACD-AHMP, the content of O, S, and H in CDA300 slightly decrease, while C and N contents increase. Thus, it is believed that the main structures of ACD and AHMP in CDA300 do not change, but are only oligomerized and slightly carbonized.

The element states of the catalysts were further investigated by X-ray photoelectron spectroscopy (XPS) spectra (Fig. S6). Based on the high resolution XPS spectra of N 1s, all samples display two different chemical states of N that belong to N-H bond at  $399.71 \text{ eV}$  and C=N-C bond at  $398.58 \text{ eV}$  [34,46]. After calcination, the intensity ratio of N-H to C=N-C decreases due to the condensation between amino groups. Based on the S 2p spectra, the S-H band at  $162.1 \text{ eV}$  is found in both CDA and CDA250 [36]. After polymerization, this peak was not detected in CDA300 and CDA350, which matches with the ATR-FTIR results and further indicates that condensation reaction occurs between AHMP. The structure of AHMP300 was also studied by XRD, ATR-FTIR and XPS analysis and the results are shown in Fig. S7.

The above analysis results confirm that CDA300 consists of ACD and AHMP, and the introduced ACD crosslinks with AHMP through Schiff base reaction. At the same time, the condensation occurs between AHMP components. Both reaction processes contribute to the forming of CDA300 polymer with unique structure and photocatalytic properties.

#### 3.2. Photoelectric properties of CDA

The  $\text{H}_2\text{O}_2$  generation performance largely depends on the photoelectric properties of the catalyst. The photoresponse range is one of the key factors for the photocatalytic performance. The ultraviolet-visible diffuse reflectance spectrum (UV-vis DRS) was obtained to investigate the optical properties of CDA300. As shown in Fig. 3a, CDA300 exhibits superior light absorption ability in visible light region. Moreover, the absorption edge of CDA300 extends to the near-infrared region, which is beneficial for the utilization of solar energy. The energy gap of CDA300 was determined to be  $2.33 \text{ eV}$  based on the Kubelka-Munk equation [47]. The band structure of was further determined through Mott-Schottky and ultraviolet photoelectron spectroscopy (UPS) measurements and the position of conduction band and valence band will determine the catalytic reaction process of  $\text{H}_2\text{O}_2$  generation. As presented in Fig. 3b, CDA300 exhibits typical n-type semiconductor feature with positive slope of Mott-Schottky plots [48]. The flat band potential ( $E_{fb}$ ) of CDA300 is  $-0.8 \text{ V}$  vs Ag/AgCl (i.e.,  $-0.3 \text{ V}$  vs RHE) according to the convergence of tangent lines. Considering that the CB value ( $E_{CB}$ ) is more negative by  $0.1 \text{ V}$  than  $E_{fb}$ , the CB value of CDA300 is calculated as  $-0.4 \text{ V}$  (vs. RHE) [49,50]. Thus, the potential of valance band ( $E_{VB}$ ) is determined to be  $1.93 \text{ V}$  (vs RHE) by  $E_g = E_{VB} - E_{CB}$ . Meanwhile, based on the UPS results (Fig. 3c), the valance band potential of CDA300 was calculated to be  $1.93 \text{ V}$  (calculation details are shown in Text S5), which is consistent with the above results. Based on the estimated band structures of CDA300 (Fig. 3d), the CB value of CDA300 is negative enough to reduce oxygen for  $\text{H}_2\text{O}_2$  generation, and the VB is also lower than the oxidation level from  $\text{H}_2\text{O}$  to  $\text{H}_2\text{O}_2$ . Therefore, this catalyst possesses unique advantages in producing  $\text{H}_2\text{O}_2$  in pure water with optimal band structure.

The photocurrent of the catalysts was collected to study the generation and separation capacity of photogenerated carriers. As displayed in Fig. 3e, CDA300 exhibits the highest photocurrent density (average value of  $0.56 \mu\text{A cm}^{-2}$ ) among the tested catalysts, indicating the highest photocatalytic activity and charge separation efficiency. The electrochemical impedance spectroscopy (EIS) was recorded (Fig. S8) to study

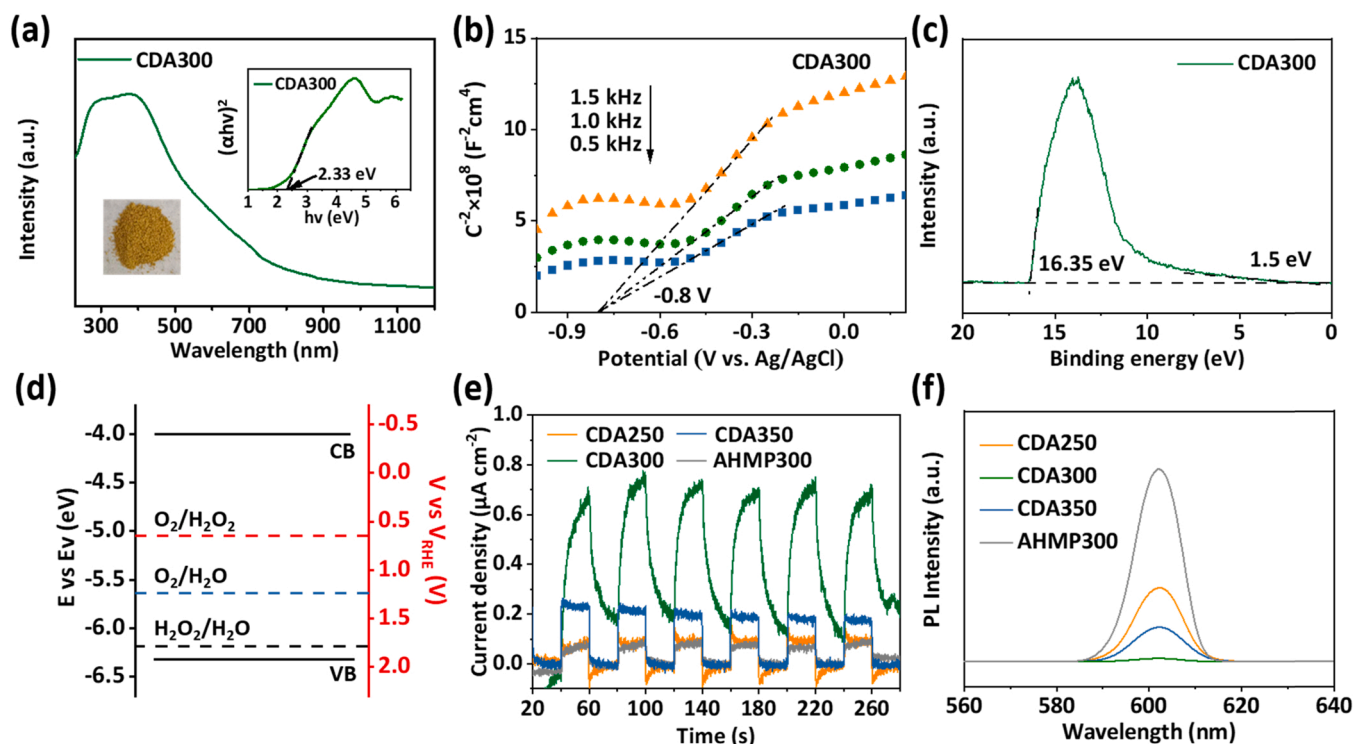


**Fig. 3.** (a) UV-Vis absorption spectra of CDA300. The insets show the energy gap of CDA300 that is estimated by the Tauc plot of  $(\alpha h\nu)^2$  vs.  $h\nu$ . The inset figure is a picture of CDA300 powder. (b) Mott-Schottky plots of CDA300 at frequencies of 0.5, 1.0, and 1.5 kHz. (c) UPS result of CDA300. (d) The estimated band structures of CDA300. (e) Transient photocurrents and (f) PL spectra of CDA and AHMP300 catalysts.

the interfacial charge transfer capacity of the catalysts. CDA300 shows the smallest charge transfer resistance among all the catalysts, indicating lowest migration resistance for the photogenerated carriers. The photoluminescence (PL) spectra of the catalysts under 300 nm excitation are shown in Fig. 3f. It is shown that the PL signal of CDA300 is very

low, suggesting that CDA300 has superior performance in suppressing the recombination of light-induced electron-hole pairs.

The unique band structure and electronic properties of CDA300 were further analyzed from the molecular level by density functional theory (DFT) calculation and time-dependent DFT (TD-DFT). The highest

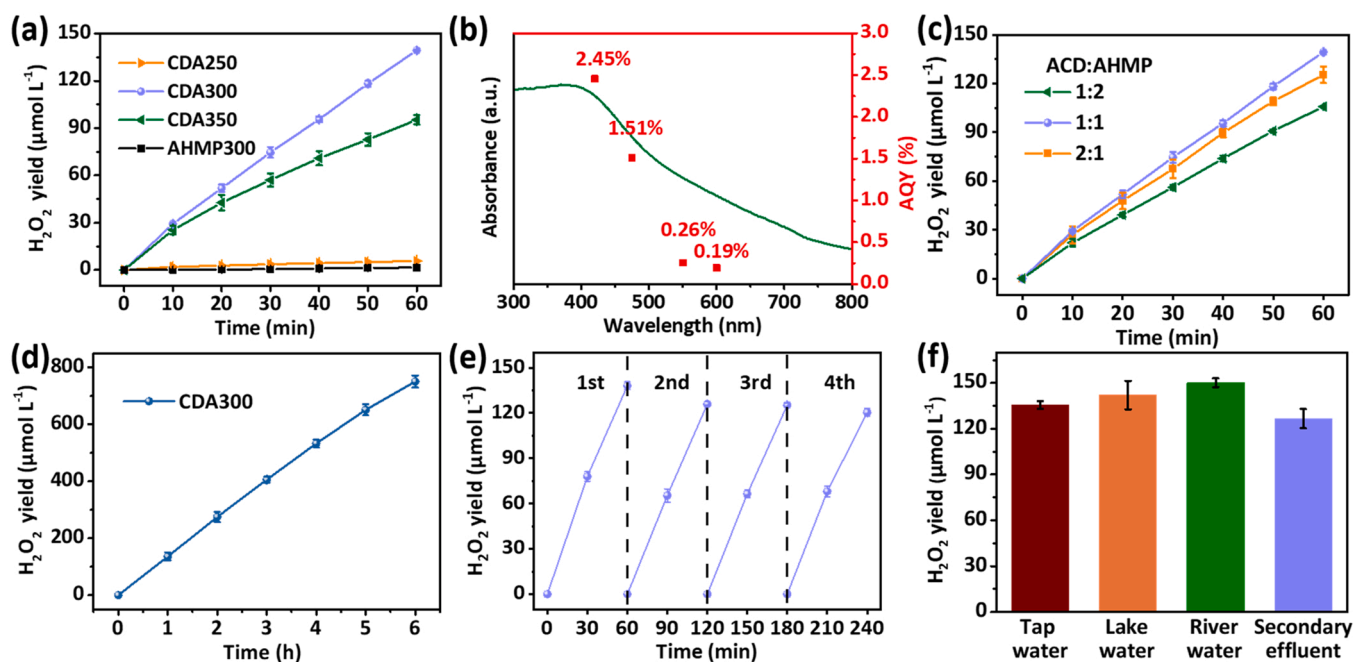


**Fig. 4.** Photocatalytic  $\text{H}_2\text{O}_2$  evolution yields of the catalysts. (b) The absorption spectra and apparent quantum yields of CDA300. (c) Comparison of  $\text{H}_2\text{O}_2$  evolution yields of CDA300 prepared with different mass ratios of the precursors (ACD: AHMP). (d) 6 h photocatalytic  $\text{H}_2\text{O}_2$  production over CDA300. (e) Cycling test of  $\text{H}_2\text{O}_2$  evolution for four continuous cycles. (f) The photocatalytic  $\text{H}_2\text{O}_2$  production over CDA300 in different water media (tap water, lake water, river water, and secondary effluent). Reaction conditions: 0.25 g/L catalyst, natural pH without adjustment, open air condition, visible light irradiation ( $\lambda \geq 420$  nm).

occupied molecular orbital (HOMO) and lowest unoccupied molecular orbital (LUMO) locations of CDA300 and AHMP300 are presented in Fig. S9. The occupied and unoccupied orbits of AHMP300 are uniformly delocalized over periodic pyrimidine ring in AHMP300. In contrast, the LUMO and HOMO of CDA300 localize on the different units and exhibit localized charge accumulation, resulting in narrowed HOMO-LUMO energy gap. It can be inferred that the spatial separation of charge carriers can be formed in CDA300, which greatly suppresses the charge recombination [51]. Moreover, the excited electronic structures and excitation energy during the S0→S1 excitation were obtained to study the charge separation ability. The TD-DFT results show that the excitation energy of CDA300 (4.084 eV) is lower than that of AHMP300 (4.435 eV), suggesting the higher charge separation efficiency.

### 3.3. Photocatalytic H<sub>2</sub>O<sub>2</sub> evolution

The photocatalytic H<sub>2</sub>O<sub>2</sub> production capacity of the catalyst was evaluated in pure water without sacrificial agent or pH adjustment in open air condition. As depicted in Fig. 4a, AHMP300 obtained by pure AHMP polycondensation shows weak H<sub>2</sub>O<sub>2</sub> production performance (1.6 μmol L<sup>-1</sup> h<sup>-1</sup>), and similar performance (5.7 μmol L<sup>-1</sup> h<sup>-1</sup>) is found for CDA250. In contrast, CDA300 exhibits superior photocatalytic performance for H<sub>2</sub>O<sub>2</sub> production (139.3 μmol L<sup>-1</sup> h<sup>-1</sup>) under the same test condition, which is ~87 times higher than that of the AHMP300. This H<sub>2</sub>O<sub>2</sub> evolution performance is also much higher than those of the other photocatalytic systems and even higher or comparable to those with sacrificial agent (Table S2). With further increase of the calcination temperature, the photocatalytic H<sub>2</sub>O<sub>2</sub> production rate of CDA350 is decreased, which is possibly because excessive polymerization of AHMP may lead to the increase in the carriers recombination rate [34]. In the photocatalytic H<sub>2</sub>O<sub>2</sub> production process, the generated H<sub>2</sub>O<sub>2</sub> will inevitably react with electrons or holes and decompose into •O<sub>2</sub> or •OH. Thus, the photocatalytic H<sub>2</sub>O<sub>2</sub> production is a dynamic process between the generation and decomposition of H<sub>2</sub>O<sub>2</sub>. Therefore, the formation (k<sub>f</sub>) and decomposition (k<sub>d</sub>) kinetics of H<sub>2</sub>O<sub>2</sub> were obtained through the following equation:

$$[H_2O_2] = \frac{k_f}{k_d} \times \{1 - \exp(-k_d \times t)\}, \quad (1)$$

where t is the reaction time (min) and [H<sub>2</sub>O<sub>2</sub>] is the concentration of produced H<sub>2</sub>O<sub>2</sub> (μmol L<sup>-1</sup>). As shown in Fig. S10, CDA300 shows the highest k<sub>f</sub> value (2.72 μmol min<sup>-1</sup>) and lowest k<sub>d</sub> value (0.00569 min<sup>-1</sup>) among all samples, indicating the excellent ability to generate H<sub>2</sub>O<sub>2</sub> and inhibit H<sub>2</sub>O<sub>2</sub> decomposition.

As shown in Fig. 4b, apparent quantum yield (AQY) of CDA300 was measured at the wavelength of 420, 475, 550, and 600 nm, respectively. The CDA300 exhibits the maximum AQY (2.45%) at 420 nm since the increasing wavelength causes fewer photons to be absorbed for photocatalysis. The solar-to-chemical conversion (SCC) efficiency of CDA300 (0.11%) is two orders higher than that of the AHMP300 (0.0015%) and is also higher or comparable with other organic photocatalysts (Table S2). The mass ratio of ACD to AHMP in CDA was studied and optimized. As shown in Fig. 4c, with mass ratios of 1:2, 1:1, and 2:1 (ACD to AHMP), the obtained polymer catalysts all exhibit high photocatalytic H<sub>2</sub>O<sub>2</sub> generation performance and the optimal ratio is 1:1.

To investigate the long-term operation performance, the photo-irradiation time was prolonged to 6 hr. As shown in Fig. 4d and Fig. S11, the generation rate is steady after 6 hr irradiation. While, the generated H<sub>2</sub>O<sub>2</sub> remains stable under dark condition in open air for 6 hr and decreases by ~25% after 54 hr. These results indicate that CDA300 has good long-term performance and the produced H<sub>2</sub>O<sub>2</sub> is stable in the system under dark condition, which presents high potential for practical applications. Cycling tests were also carried out to evaluate the photostability of the catalyst (Fig. 4e). After 4 cycles of operation, the photocatalytic H<sub>2</sub>O<sub>2</sub> production yield of CDA300 only slightly decreases. To

study the structure and properties of the sample after the reaction, the used CDA300 after 4 cycles was characterized by XRD, FT-IR, and XPS analysis. As shown in Fig. S12, the fresh and used CDA300 show very similar results in these analysis tests, confirming the good stability of the polymer catalyst during the reaction.

The photocatalytic H<sub>2</sub>O<sub>2</sub> production performance was further tested in different water bodies to investigate its applicability in practical applications. As shown in Fig. 4f, CDA300 maintains high yields in actual water bodies including tap water, lake water, river water, and secondary effluent. Meanwhile, using lake water and secondary effluent as the representative reaction solution, the photocatalytic sterilization effect of CDA300 on bacteria was studied. As shown in Fig. S13a, after 60 min of irradiation, the number of bacteria on agar culture is significantly reduced, confirming the high bacterial inhibition ability. Moreover, as shown in Fig. S13b, CDA300 also shows high photocatalytic sterilization ability for secondary biologically treated effluent, indicating that the catalyst has potential for practical wastewater treatment. The above results reveal that CDA300 can be applied for photocatalytic H<sub>2</sub>O<sub>2</sub> evolution in actual water bodies to realize in-situ sterilization at low catalyst dosage (0.25 g/L) under visible light illumination.

### 3.4. Reaction mechanism

A series of experiments were carried out to investigate the reaction mechanism of photocatalytic H<sub>2</sub>O<sub>2</sub> production by CDA300. The photocatalytic H<sub>2</sub>O<sub>2</sub> production in pure water system mainly consists of two pathways [52], i.e., single-electron or two-electron oxygen reduction reaction (Eqs. 2–4) and two-electron water oxidation (Eq. 5).



It is shown that oxygen, water, and protons play decisive roles in the process of photocatalytic H<sub>2</sub>O<sub>2</sub> evolution. Therefore, at first, we studied the photocatalytic H<sub>2</sub>O<sub>2</sub> production over CDA300 under different atmospheres including O<sub>2</sub>, air, and Ar. As shown in Fig. 5a. Compared with air atmosphere, the H<sub>2</sub>O<sub>2</sub> production rate slightly increases in the O<sub>2</sub>-saturated system, while the production rate greatly decreases (but not to zero) in Ar atmosphere. These results indicate that photocatalytic H<sub>2</sub>O<sub>2</sub> evolution over CDA300 may proceed through both ORR and WOR processes.

The O<sub>2</sub> temperature-programmed desorption (TPD) measurement was carried out to investigate the interaction between oxygen and photocatalyst. The insufficient interaction between oxygen and photocatalyst is one of the bottlenecks in the ORR process for H<sub>2</sub>O<sub>2</sub> production. As shown in Fig. 5b, CDA300 shows much stronger oxygen adsorption capacity than that of AHMP300. The introduction of ACD could be the main reason for the improvement of oxygen adsorption, since the hydrophobic cavity of ACD can serve as the oxygen transport channel [33]. Moreover, it is proposed that oxygen transported by ACD can be utilized directly and efficiently at adjacent sites, which is demonstrated by DFT simulation. As shown in Fig. 6a-b, two possible active sites (C1 atom in AHMP dimer and C2 atom in AHMP) for ORR process were investigated, and the ORR intermediates (\*OOH) was identified. Based on the Gibbs free energy, the C1 site has lower energy barrier than that of the C2 site as the \*OOH is easier to be activated at C1 site, indicating the oxygen transferred to the C1 site through the ACD cavity can be directly reduced to generate H<sub>2</sub>O<sub>2</sub>. The reaction process of oxygen adsorption at C1 active site to generate H<sub>2</sub>O<sub>2</sub> is illustrated in Fig. 6c.

The photocatalytic hydrogen evolution capacity of CDA300 was evaluated to explore the possible competitive hydrogen production

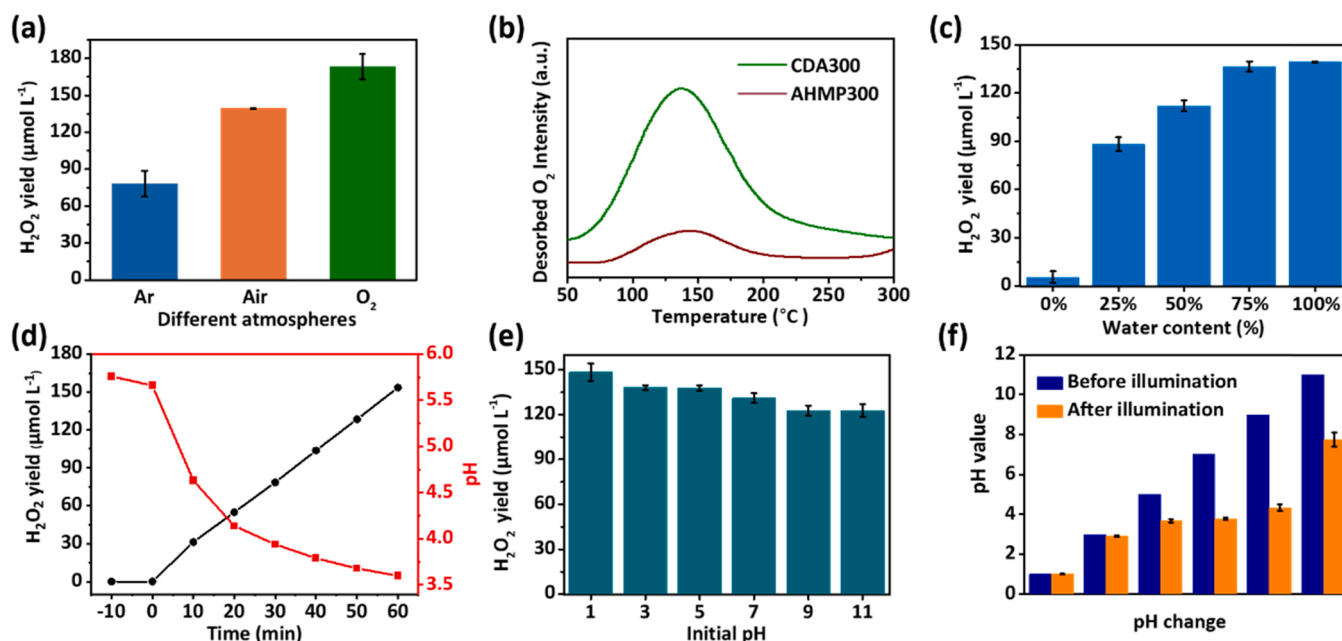


**Fig. 5.** (a) Effect of different atmospheres on the H<sub>2</sub>O<sub>2</sub> generation with CDA300 (0.25 g/L catalyst). (b) The O<sub>2</sub>-TPD capturing ability of CDA300 and AHMP300. (c) Comparison of photocatalytic H<sub>2</sub>O<sub>2</sub> generation over CDA300 in different proportions of water/acetonitrile mixture in open air (0.25 g/L catalyst). (d) The pH evolution and corresponding H<sub>2</sub>O<sub>2</sub> yield of the CDA300 system at initial pH of 5.76. (e) Photocatalytic H<sub>2</sub>O<sub>2</sub> evolution over CDA300 in pure water at different pH in open air (0.25 g/L catalyst). (f) The pH changes at different initial pH before and after photo irradiation for 60 min.

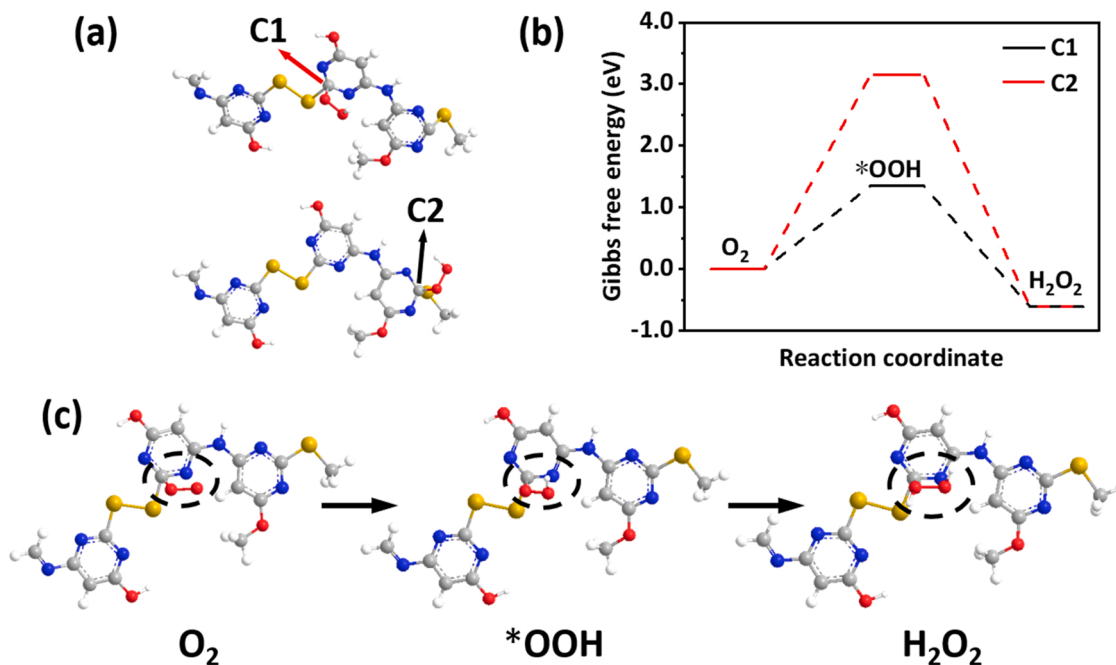


**Fig. 6.** (a) Two possible binding sites of \*OOH intermediate in CDA300. (b) Calculated free energy diagrams of oxygen reduction pathway towards H<sub>2</sub>O<sub>2</sub> production on different active sites in CDA300. (c) Schematic diagram of oxygen reduction to H<sub>2</sub>O<sub>2</sub> on C1 cite of CDA300.

reaction and H<sub>2</sub>O<sub>2</sub> generation reaction. As shown in Fig. S14, almost no H<sub>2</sub> is produced under visible light illumination at oxygen saturation condition. The competition between these two processes may be affected by the mass transfer ability of oxygen, pH value, and the available active sites for these two reactions [53,54]. The CDA300 shows much stronger oxygen adsorption capacity, so that the oxygen in water is easily transferred to the C atom active sites through the ACD cavity for H<sub>2</sub>O<sub>2</sub> generation, which inhibits the photocatalytic H<sub>2</sub> evolution. Moreover, neutral pH and no suitable active site in CDA300 for H<sup>+</sup>

reduction may also account for the low efficiency of photocatalytic H<sub>2</sub> generation [24].

Subsequently, ultrapure water was replaced by acetonitrile with different contents to confirm the role of water in the system. As displayed in Fig. 5c, almost no H<sub>2</sub>O<sub>2</sub> is generated in 100% acetonitrile solution, and once water is added, the photocatalytic yield rate of H<sub>2</sub>O<sub>2</sub> increases and reaches the maximum generation rate when pure water is used. This result suggests that H<sub>2</sub>O is of great significance for this system and it works as the electron donor to consume photogenerated holes.



As reported, acidic pH is beneficial to the generation of  $\text{H}_2\text{O}_2$  due to the necessity of  $\text{H}^+$  for ORR process, while alkaline pH will suppress this process [55]. Generally, the initial pH of ultrapure water and actual water bodies is around 6–8, which is not conducive to the generation of  $\text{H}_2\text{O}_2$ . Therefore, the pH changes were monitored during the  $\text{H}_2\text{O}_2$  production in this system to elucidate the reason for superior performance of CDA300. As shown in the Fig. 5d, the initial pH of ultrapure water is 5.76, which decreases in dark condition with CDA300. When the reaction solution exposed to light, the pH drops rapidly and is eventually reaches 3.6 after 60 min irradiation. The decrease in pH may be attributed to the proton produced by the oxidation of water by photoinduced holes. When the pH decreases, the evolution rate of  $\text{H}_2\text{O}_2$  increases, which confirms that low pH is benefit for the photocatalytic  $\text{H}_2\text{O}_2$  generation. This result can explain the high evolution rate of  $\text{H}_2\text{O}_2$  over CDA300 in neutral pH water. As shown in Fig. 5e, the CDA300 system can maintain outstanding  $\text{H}_2\text{O}_2$  production rates under different pH conditions even up to pH 11. As exhibited in Fig. 5f, the pH values of the reaction solution with different initial pH are reduced after 60 min irradiation. The above results confirm that the CDA300 catalysis system can be adapted to the actual water bodies and sewage in different pH conditions, which has high application promise for different water systems.

To further understand the role of radicals in the reaction process, free radical trapping experiments were performed. Considering that superoxide radical ( $\cdot\text{O}_2^-$ ) is the main intermediate product in ORR process, p-benzoquinone (p-BQ) was used to as scavenger of  $\cdot\text{O}_2^-$ . As shown in Fig. 7a, with the addition of 1 mM p-BQ, the photocatalytic evolution rate decreases dramatically, which indicates the importance role of  $\cdot\text{O}_2^-$  and ORR during the  $\text{H}_2\text{O}_2$  generation. The DMPO spin-trapping ESR results in Fig. S15 show characteristic signals of DMPO- $\cdot\text{O}_2^-$  in the

reaction solution after 10 min irradiation, which matches with the results of  $\cdot\text{O}_2^-$  quenching experiment. Tert-butyl alcohol (TBA) and EDTA-2Na were used as the scavenger of hydroxyl radical ( $\cdot\text{OH}$ ) and hole ( $\text{h}^+$ ), respectively. The photocatalytic performance slightly decreases with EDTA-2Na, while no obvious change is found with TBA, suggesting that  $\text{h}^+$  plays an important role in the photocatalytic reaction, while  $\cdot\text{OH}$  is not involved. In other words,  $\text{H}_2\text{O}_2$  can be directly generated by oxidizing water by photoinduced holes through a two-electron WOR process, rather than by  $\cdot\text{OH}$  [56,57].

The electron transfer number (n) of ORR and WOR was determined by rotating disk electrode (RDE) and rotating ring-disk electrode (RRDE) tests, respectively. Based on the LSV results of CDA300 (Fig. 7b), the fitted Koutecky-Levich plots was obtained to calculate the n value for ORR process. The obtained n value of 2.02 confirms the two-electron ORR process in the photocatalytic reaction. Based on the RRDE results (Fig. 7c), the n value of WOR process is determined to be 1.76, which reveals that the WOR process involves two-electron oxidation pathway to form  $\text{H}_2\text{O}_2$ . The formation of oxygen intermediate  $\cdot\text{OH}$  is the key step in the formation of  $\text{H}_2\text{O}_2$  by two-electron water oxidation. Previous studies have shown that  $\Delta G_{\cdot\text{OH}}$  between 1.6 eV and 2.4 eV favors the two-electron formation of  $\text{H}_2\text{O}_2$ , while  $\Delta G_{\cdot\text{OH}} < 1.6$  eV or  $> 2.4$  eV favors the formation of  $\text{O}_2$  or  $\cdot\text{OH}$  radicals, respectively [26,58]. The calculation results (Fig. S16) show that  $\cdot\text{OH}$  is favorable to form on the pyrimidine ring of CDA300 with the  $\Delta G_{\cdot\text{OH}}$  value of 1.95 eV, which may result in the  $\text{H}_2\text{O}_2$  generation through a selective two-electron WOR process.

In-situ FT-IR measurements were conducted to further analyze the oxygen intermediates on the surface of CDA300. As shown in Fig. S17, the molecular oxygen  $\text{O}_{2(\text{ad})}$  and  $\text{H}_2\text{O}_{(\text{ad})}$  adsorbed on CDA300 can be found at  $1454\text{ cm}^{-1}$  and  $1647\text{ cm}^{-1}$ , respectively [59]. Under visible

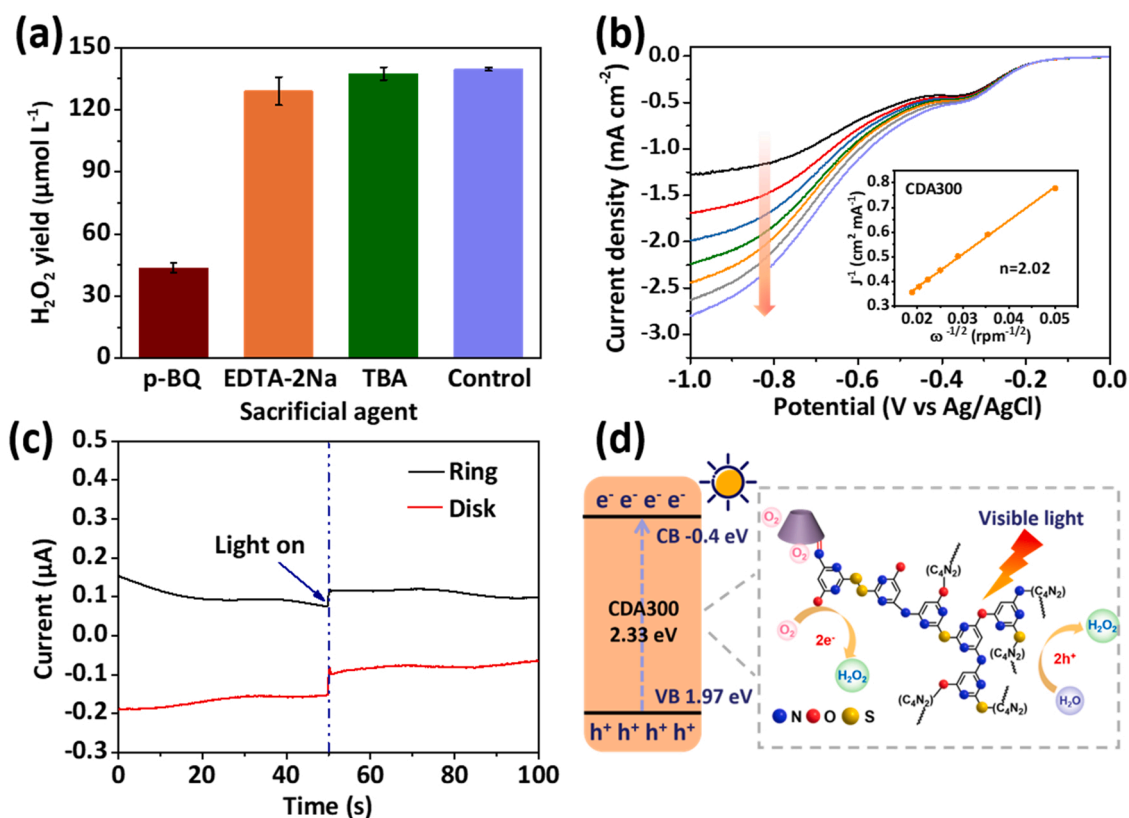


Fig. 7. (a) Quenching experiments on photocatalytic  $\text{H}_2\text{O}_2$  production over CDA300 with p-BQ (1 mM), EDTA-2Na (1 mM), and TBA (1 mM). Reaction conditions: 0.25 g/L of catalysts, natural pH without adjustment, open air condition, visible light irradiation ( $\lambda \geq 420$  nm). (b) LSV curves of CDA300 measured on RDE at different rotating speeds ( $\text{O}_2$ -saturated 0.1 M  $\text{Na}_2\text{SO}_4$  solution). Inset: the corresponding Koutecky-Levich plots. (c) RRDE i-t curves of CDA300 in dark and visible light at a rotating speed of 1600 rpm in Ar-saturated 0.1 M  $\text{Na}_2\text{SO}_4$  solution. (d) Schematic diagram of the reaction pathway of photocatalytic  $\text{H}_2\text{O}_2$  production with CDA300.



light illumination, two new peaks corresponding to the absorbed  $\text{OOH}_{(\text{ad})}$  and  $\text{OH}_{(\text{ad})}$  intermediate appear at  $1267\text{ cm}^{-1}$  and  $1047\text{ cm}^{-1}$ , respectively [26,60]. Thus, the presence of the key oxygen intermediate  $^*\text{OOH}$  in the  $2\text{e}^-$  ORR process and  $^*\text{OH}$  in the  $2\text{e}^-$  WOR process clearly confirms the two-channel reaction pathway of  $\text{H}_2\text{O}_2$  generation over CDA300, which is consistent with the DFT simulation results.

Base on the mechanism investigation, we propose a reaction pathway of photocatalytic  $\text{H}_2\text{O}_2$  evolution over CDA300 (Fig. 7d). When exposed to visible light, the polymer catalyst CDA300 is excited to produce photoinduced electron hole pairs. The DFT simulation results show that the unique structure of CDA300 endows it with high charge separation efficiency. The oxygen in water migrates to the C atom of AHMP through the ACD cavity, and is reduced by electrons to generate  $\text{H}_2\text{O}_2$ . While, the holes remain in the valence band generate  $\text{H}_2\text{O}_2$  by oxidizing water through a  $2\text{e}^-$  WOR process, in which the pyrimidine ring of CDA300 is beneficial for the formation of key intermediates ( $^*\text{OH}$ ) for  $\text{H}_2\text{O}_2$  generation. The simultaneous occurrence of ORR and WOR processes not only inhibits the recombination of photogenerated carriers, but also achieves high production efficiency of  $\text{H}_2\text{O}_2$ .

#### 4. Conclusion

In this study, a novel metal-free polymer catalyst is synthesized by thermal condensation of ACD-AHMP crosslinking product, which can efficiently generate  $\text{H}_2\text{O}_2$  from water through photocatalysis without oxygen aeration and sacrificial agent. The incorporation of cyclodextrin in the framework of CDA300 enhances the oxygen adsorption capacity. Due to the wide light absorption range and appropriate band structure, the reported photocatalyst achieves superior photocatalytic  $\text{H}_2\text{O}_2$  generation performance through a dual-channel pathway (two-electron ORR and two-electron WOR). Since a large amount of  $\text{H}^+$  is produced in the WOR process, this catalysis system exhibits excellent pH adaptability and can produce  $\text{H}_2\text{O}_2$  even under alkaline condition. This catalyst also displays outstanding stability, which can be applied to photocatalytic  $\text{H}_2\text{O}_2$  generation in various water bodies. This work provides new insights in organic polymer photocatalyst for  $\text{H}_2\text{O}_2$  generation and contributes to the development of novel catalyst for water remediation and energy conversion.

#### CRedit authorship contribution statement

**Chengcheng Chu:** Conceptualization; Data curation; Formal analysis; Investigation; Methodology; Validation; Writing – original draft. **Qiuju Li:** Data curation; Formal analysis; Investigation; Methodology. **Wei Miao:** Data curation; Formal analysis; Investigation; Methodology. **Hehe Qin:** Data curation; Formal analysis; Investigation; Methodology. **Xinru Liu:** Data curation; Formal analysis; Investigation; Methodology. **Ducheng Yao:** Data curation; Formal analysis; Investigation; Methodology. **Shun Mao (corresponding author):** Conceptualization; Investigation; Funding acquisition; Project administration; Resources; Supervision; Writing - review & editing.

#### Declaration of Competing Interest

The authors declare that they have no known competing financial interests or personal relationships that could have appeared to influence the work reported in this paper.

#### Acknowledgements

This work was supported by the National Key R&D Program of China (2019YFC1905400).

#### Appendix A. Supporting information

Supplementary data associated with this article can be found in the

online version at doi:10.1016/j.apcatb.2022.121485.

#### References

- [1] L. Zhou, J. Feng, B. Qiu, Y. Zhou, J. Lei, M. Xing, L. Wang, Y. Zhou, Y. Liu, J. Zhang, Appl. Catal. B: Environ. 267 (2020), 118396.
- [2] J. Cai, J. Huang, S. Wang, J. Iocozzia, Z. Sun, J. Sun, Y. Yang, Y. Lai, Z. Lin, Adv. Mater. 31 (2019), e1806314.
- [3] H.-i Kim, O.S. Kwon, S. Kim, W. Choi, J.-H. Kim, Energy Environ. Sci. 9 (2016) 1063–1073.
- [4] C. Chu, Q. Zhu, Z. Pan, S. Gupta, D. Huang, Y. Du, S. Weon, Y. Wu, C. Muhich, E. Stavitski, K. Domen, J.H. Kim, Proc. Natl. Acad. Sci. U. S. A. 117 (2020) 6376–6382.
- [5] H. Hou, X. Zeng, X. Zhang, Angew. Chem. Int. Ed. 59 (2020) 17356–17376.
- [6] Y. Xue, Y. Wang, Z. Pan, K. Sayama, Angew. Chem. Int. Ed. 60 (2021) 10469–10480.
- [7] T.M. Gill, L. Vallez, X. Zheng, ACS Energy Lett. 6 (2021) 2854–2862.
- [8] J. Cao, H. Wang, Y. Zhao, Y. Liu, Q. Wu, H. Huang, M. Shao, Y. Liu, Z. Kang, J. Mater. Chem. A 8 (2020) 3701–3707.
- [9] B. Li, S. Yu, M. Zhou, C. Chen, C. Lai, M. Zhang, H. Lin, J. Mater. Chem. A 10 (2022) 3905–3932.
- [10] X. Chen, Y. Kuwahara, K. Mori, C. Louis, H. Yamashita, J. Mater. Chem. A 9 (2021) 2815–2821.
- [11] J. Zhang, L. Zheng, F. Wang, C. Chen, H. Wu, S.A.K. Leghari, M. Long, Appl. Catal. B: Environ. 269 (2020), 118770.
- [12] K. Fuku, R. Takioka, K. Iwamura, M. Todoroki, K. Sayama, N. Ikenaga, Appl. Catal. B: Environ. 272 (2020), 119003.
- [13] G.-h Moon, W. Kim, A.D. Bokare, N.-e Sung, W. Choi, Energy Environ. Sci. 7 (2014) 4023–4028.
- [14] Z. Zhu, H. Pan, M. Murugananthan, J. Gong, Y. Zhang, Appl. Catal. B: Environ. 232 (2018) 19–25.
- [15] C. Feng, L. Tang, Y. Deng, J. Wang, J. Luo, Y. Liu, X. Ouyang, H. Yang, J. Yu, J. Wang, Adv. Funct. Mater. 30 (2020), 2001922.
- [16] Y. Shiraishi, S. Kanazawa, Y. Kofuji, H. Sakamoto, S. Ichikawa, S. Tanaka, T. Hirai, Angew. Chem. Int. Ed. 53 (2014) 13454–13459.
- [17] L. Shi, L. Yang, W. Zhou, Y. Liu, L. Yin, X. Hai, H. Song, J. Ye, Small 14 (2018), 1703142.
- [18] L. Zhou, J. Lei, F. Wang, L. Wang, M.R. Hoffmann, Y. Liu, S.-I. In, J. Zhang, Appl. Catal. B: Environ. 288 (2021), 119993.
- [19] C. Chu, W. Miao, Q. Li, D. Wang, Y. Liu, S. Mao, Chem. Eng. J. 428 (2022), 132531.
- [20] Y. Yang, Z. Zeng, G. Zeng, D. Huang, R. Xiao, C. Zhang, C. Zhou, W. Xiong, W. Wang, M. Cheng, W. Xue, H. Guo, X. Tang, D. He, Appl. Catal. B: Environ. 258 (2019), 117956.
- [21] X. Zhao, Y. You, S. Huang, Y. Wu, Y. Ma, G. Zhang, Z. Zhang, Appl. Catal. B: Environ. 278 (2020), 119251.
- [22] X. Chen, W. Zhang, L. Zhang, L. Feng, C. Zhang, J. Jiang, T. Yan, H. Wang, J. Mater. Chem. A 8 (2020) 18816–18825.
- [23] C. Feng, L. Tang, Y. Deng, J. Wang, Y. Liu, X. Ouyang, H. Yang, J. Yu, J. Wang, Appl. Catal. B: Environ. 281 (2021), 119539.
- [24] P. Zhang, Y. Tong, Y. Liu, J.J.M. Vequizo, H. Sun, C. Yang, A. Yamakata, F. Fan, W. Lin, X. Wang, W. Choi, Angew. Chem. Int. Ed. 59 (2020) 16209–16217.
- [25] T. Mahvelati-Shamsabadi, H. Fattahimoghaddam, B.-K. Lee, H. Ryu, J.I. Jang, Chem. Eng. J. 423 (2021), 130067.
- [26] L. Chen, L. Wang, Y. Wan, Y. Zhang, Z. Qi, X. Wu, H. Xu, Adv. Mater. 32 (2020), e1904333.
- [27] C. Krishnaraj, H. Sekhar Jena, L. Bourda, A. Laemont, P. Pachfule, J. Roeser, C. V. Chandran, S. Borgmans, S.M.J. Rogge, K. Leus, C.V. Stevens, J.A. Martens, V. Van Speybroeck, E. Breynaert, A. Thomas, P. Van Der Voort, J. Am. Chem. Soc. 142 (2020) 20107–20116.
- [28] C. Dai, T. He, L. Zhong, X. Liu, W. Zhen, C. Xue, S. Li, D. Jiang, B. Liu, Adv. Mater. Interfaces 8 (2021), 2002191.
- [29] J. Han, Z. Zhu, N. Li, D. Chen, Q. Xu, H. Li, J. He, J. Lu, Appl. Catal. B: Environ. 291 (2021), 120108.
- [30] J. Yang, J. Jing, Y. Zhu, Adv. Mater. 33 (2021), e2101026.
- [31] Y. Shiraishi, T. Takii, T. Hagi, S. Mori, Y. Kofuji, Y. Kitagawa, S. Tanaka, S. Ichikawa, T. Hirai, Nat. Mater. 18 (2019) 985–993.
- [32] H. Kim, K. Shim, K.E. Lee, J.W. Han, Y. Zhu, W. Choi, Appl. Catal. B: Environ. 299 (2021), 120666.
- [33] H. Zhu, Q. Xue, G. Zhu, Y. Liu, X. Dou, X. Yuan, J. Mater. Chem. A 9 (2021) 6872–6880.
- [34] J. Li, N. Karjule, J. Qin, Y. Wang, J. Barrio, M. Shalom, Molecules 26 (2021) 1646.
- [35] J. Barrio, N. Karjule, J. Qin, M. Shalom, ChemCatChem 11 (2019) 6295–6300.
- [36] Q. Li, D. Wang, X. Fang, B. Zong, Y. Liu, Z. Li, S. Mao, K.K. Ostrikov, Chem. Commun. 57 (2021) 1161–1164.
- [37] S. Guo, H. Zhang, Y. Chen, Z. Liu, B. Yu, Y. Zhao, Z. Yang, B. Han, Z. Liu, ACS Catal. 8 (2018) 4576–4581.
- [38] F. Qin, J. Li, C. Zhang, G. Zeng, D. Huang, X. Tan, D. Qin, H. Tan, Sci. Total Environ. (2021), 151774.
- [39] Z. Hu, Y. Huang, X. He, W. Guo, K. Yan, Chem. Eng. J. 427 (2022), 131464.
- [40] F. Qin, Y. Peng, G. Song, Q. Fang, R. Wang, C. Zhang, G. Zeng, D. Huang, C. Lai, Y. Zhou, X. Tan, M. Cheng, S. Liu, J. Hazard. Mater. 398 (2020), 122816.
- [41] E. Garcia-Diaz, D. Zhang, Y. Li, R. Verduzco, P.J.J. Alvarez, Water Res 183 (2020), 116095.
- [42] V.H. Pham, T.P.D. Phan, D.C. Phan, B.D. Vu, Molecules 25 (2020) 324.

- [43] S.A. Elsayed, B.J. Jean-Claude, I.S. Butler, S.I. Mostafa, J. Mol. Struct. 1028 (2012) 208–214.
- [44] M. Shunmughanathan, N. Madankumar, K. Pitchumani, ChemistrySelect 3 (2018) 13743–13750.
- [45] A. Alsaiee, B.J. Smith, L. Xiao, Y. Ling, D.E. Helbling, W.R. Dichtel, Nature 529 (2016) 190–194.
- [46] F. Qin, C. Zhang, G. Zeng, D. Huang, X. Tan, A. Duan, Renew. Sust. Energ. Rev. 157 (2022), 112056.
- [47] D. Wang, Q. Li, W. Miao, Y. Liu, N. Du, S. Mao, Chem. Eng. J. 402 (2020), 126211.
- [48] W. Miao, Y. Wang, Y. Liu, H. Qin, C. Chu, S. Mao, Engineering (2022), <https://doi.org/10.1016/j.eng.2021.12.016>.
- [49] J. Xiong, X. Li, J. Huang, X. Gao, Z. Chen, J. Liu, H. Li, B. Kang, W. Yao, Y. Zhu, Appl. Catal. B: Environ. 266 (2020), 118602.
- [50] B. Li, C. Lai, H. Lin, S. Liu, L. Qin, M. Zhang, M. Zhou, L. Li, H. Yi, L. Chen, Chem. Eng. J. 431 (2022), 134044.
- [51] D. Zhao, C.L. Dong, B. Wang, C. Chen, Y.C. Huang, Z. Diao, S. Li, L. Guo, S. Shen, Adv. Mater. 31 (2019), e1903545.
- [52] J. Luo, Y. Liu, C. Fan, L. Tang, S. Yang, M. Liu, M. Wang, C. Feng, X. Ouyang, L. Wang, L. Xu, J. Wang, M. Yan, ACS Catal. 11 (2021) 11440–11450.
- [53] A. Li, Q. Cao, G. Zhou, B. Schmidt, W. Zhu, X. Yuan, H. Huo, J. Gong, M. Antonietti, Angew. Chem. Int. Ed. 58 (2019) 14549–14555.
- [54] Y.C. Hao, L.W. Chen, J. Li, Y. Guo, X. Su, M. Shu, Q. Zhang, W.Y. Gao, S. Li, Z.L. Yu, L. Gu, X. Feng, A.X. Yin, R. Si, Y.W. Zhang, B. Wang, C.H. Yan, Nat. Commun. 12 (2021) 2682.
- [55] G.-h Moon, M. Fujitsuka, S. Kim, T. Majima, X. Wang, W. Choi, ACS Catal. 7 (2017) 2886–2895.
- [56] Y. Zhao, Y. Liu, J. Cao, H. Wang, M. Shao, H. Huang, Y. Liu, Z. Kang, Appl. Catal. B: Environ. 278 (2020), 119289.
- [57] J. Cao, Q. Wu, Y. Zhao, K. Wei, Y. Li, X. Wang, F. Liao, H. Huang, M. Shao, Y. Liu, Z. Kang, Appl. Catal. B: Environ. 285 (2021), 119817.
- [58] J.H. Baek, T.M. Gill, H. Abroshan, S. Park, X. Shi, J. Nørskov, H.S. Jung, S. Siahrostami, X. Zheng, ACS Energy Lett. 4 (2019) 720–728.
- [59] Y. Wang, Y. Zhou, Y. Feng, X.Y. Yu, Adv. Funct. Mater. (2022), 2110734.
- [60] H. Li, P. Wen, D.S. Itanze, Z.D. Hood, S. Adhikari, C. Lu, X. Ma, C. Dun, L. Jiang, D. L. Carroll, Y. Qiu, S.M. Geyer, Nat. Commun. 11 (2020) 3928.